

Transient State Monitoring by Total Internal Reflection Fluorescence Microscopy

Thiemo Spielmann,[†] Hans Blom,[†] Matthias Geissbuehler,[‡] Theo Lasser,[‡] and Jerker Widengren^{*,†}

Experimental Biomolecular Physics, Department of Applied Physics, Royal Institute of Technology, Albanova University Center, 106 91 Stockholm, Sweden, and Laboratoire d'Optique Biomédicalé, Ecole Polytechnique Fédérale de Lausanne (EPFL), 1015 Lausanne, Switzerland

Received: November 20, 2009; Revised Manuscript Received: January 15, 2010

Triplet, photo-oxidized and other photoinduced, long-lived states of fluorophores are sensitive to the local environment and thus attractive for microenvironmental imaging purposes. In this work, we introduce an approach where these states are monitored in a total internal reflection (TIR) fluorescence microscope, via the characteristic variations of the time-averaged fluorescence occurring in response to different excitation modulation schemes. The surface-confined TIR excitation field generates a signal from the fluorescent molecules close to the glass surface. Thereby, a high selectivity and low background noise is obtained, and in combination with low duty cycles of excitation, the overall photodegradation of the fluorescent molecules of the sample can be kept low. To verify the approach, the kinetics of the triplet and radical states of the dye Rhodamine 110 were imaged and analyzed in aqueous solutions at different concentrations of dissolved oxygen and of the reducing agent ascorbic acid. The experimental results were compared to data from corresponding fluorescence correlation spectroscopy (FCS) measurements and simulations based on finite element analysis. The approach was found to accurately determine relative populations and dynamics of triplet and photo-oxidized states, overcoming passage time limitations seen in FCS measurements. The method circumvents the need for time resolution in the fluorescence detection, allowing simultaneous readout over the whole surface area subject to excitation. It can be applied over a broad range of concentrations and does not require a strong fluorescence brightness of the sample molecules. Given the sensitivity of the triplet and photo-oxidized states to oxygen concentrations and not the least to local redox environments, we expect the approach to become an attractive tool for imaging cell metabolism.

Introduction

For many applications in fluorescence spectroscopy and imaging, a high readout rate or a high sensitivity is required. For these applications, it is important to optimize the fluorescence signal and its information content. To increase information content, multiplexing by simultaneous registration of several independent parameters has evolved as an important means in wide-field and confocal fluorescence microscopy,¹ for readouts of DNA and protein microarrays,² as well as in single-molecule spectroscopy³ and imaging.⁴ Attention has been addressed to photophysical properties determining the fluorescence saturation properties and photostabilities of the fluorophore marker molecules. Long-lived, photoinduced states, such as triplet, photoisomerized, and photo-oxidized states, are often found to reduce the signal in fluorescence microscopy⁵ and can act as precursor states of photobleaching.^{6,7} Additionally, in single-molecule experiments, their blinking may shadow other molecular processes of interest, taking place in the same time range. However, photoinduced transient states of fluorophores and fluorescent proteins have lately also attracted a large interest in biomolecular research. Photoswitching into long-lived transient states can be exploited for protein transport and localization studies in cells⁸ and provides the core mechanism in practically all recently developed approaches for fluorescence-based ultra-

high-resolution microscopy.^{9–12} Moreover, the population kinetics of long-lived photoinduced transient states also represents additional dimensions of fluorescence information. While the fluorescence lifetime of a singlet excited state of a fluorophore is $\sim 10^{-9}$ s, the lifetimes of photoinduced, non- or weakly fluorescent transient states generated by trans–cis isomerization, intersystem crossing, or photoinduced charge transfer are $\sim 10^{-6}$ – 10^{-3} s. Consequently, these states have $\sim 10^3$ – 10^6 more time to interact with the immediate environment of the fluorophore. These states can thus reflect relatively less frequent collisional interactions and can change considerably due to small changes in, for example, the accessibility of quencher molecules or in microviscosities. Still, and largely due to methodological constraints, the population dynamics of these states have to date been exploited only to a very limited extent as readout parameters in biomolecular research. Transient absorption spectroscopy has been extensively used to characterize a range of transient states and their kinetics.^{13–15} Nevertheless, the technique is technically relatively complicated, lacks the sensitivity for measurements at low ($<\mu\text{M}$) concentrations, and is mainly restricted to cuvette experiments. The emission originating either directly (phosphorescence) or indirectly (delayed fluorescence) from a long-lived first excited triplet state can also be used to characterize its population.^{16,17} This has also been implemented for microscopic imaging.¹⁸ However, coupled to the long-lived emission is also the susceptibility of the triplet state to dynamic quenching by oxygen and trace impurities, which can be circumvented only after elaborate and careful sample preparation. This artifactual quenching shortens the

* To whom correspondence should be addressed. Phone: +46855378030. E-mail: jerker@biomolphysics.kth.se.

[†] Albanova University Center.

[‡] Laboratoire d'Optique Biomédicalé, Ecole Polytechnique Fédérale de Lausanne.

triplet lifetime and makes the luminescence practically undetectable. Biomolecular monitoring by this readout is thus largely restricted to deoxygenized, carefully prepared samples, which restricts its biological applicability. For isomerized or photo-oxidized states, there is normally no alternative emission available.

As an alternative, the population and kinetics of transient states of fluorophores can be followed by fluorescence correlation spectroscopy (FCS), via the fluorescence fluctuations generated as individual fluorophores transit to and from the (non- or weakly fluorescent) transient state. The experimental realization is relatively simple, and a favorable combination of a high signal level (given by the readout of fluorescence photons) and an outstanding environmental sensitivity (given by the long lifetimes of the transient states) can be obtained. FCS measurements have proven useful for monitoring several different photoinduced transient states, including triplet states,^{19,20} isomerized states,²¹ and states generated by photoinduced charge transfer.^{22,23} These states in turn reflect a range of environmental properties, including oxygen and other quencher molecule concentrations, viscosity, local redox environments, and temperature. Transient state parameters, monitored by FCS, can also be used as a measure of the extent to which fluorescence (or Förster) resonance energy transfer (FRET) occurs between two fluorophores, reflecting intra- or intermolecular distances.²⁴ Typically, FCS measurements are performed with a confocal detection volume. For surface studies, on the other hand, objective-based total internal reflection (TIR) fluorescence excitation can provide an attractive alternative, offering higher fluorescence collection efficiencies,^{25,26} and was also recently introduced to investigate triplet-state properties of fluorophores close to dielectric surfaces.²⁷

The FCS concept for transient state monitoring is applicable to a wide range of samples. However, all forms of fluorescence fluctuation spectroscopy rely on spontaneous fluctuations of individual molecules. Thus, only very few molecules ($\sim 10^3$) can be detected at a time, and the approaches depend on a high fluorescence brightness of the molecules investigated as well as a high detection sensitivity.²⁸ TIR-mediated evanescent field excitation, combined with a highly sensitive fluorescence detection by an electron-multiplied charge-coupled device (EM-CCD) camera, has been shown to allow both autocorrelation^{29,30} and, more recently, also cross-correlation fluctuation analyses of molecular diffusion and transport in molecular membranes.³¹ However, while sufficient for relatively slow dynamics, transient state fluctuations typically take place in the μs time range and require a time resolution far beyond that of an EMCCD camera. Such a time resolution in combination with high detection sensitivity allows, up to date, only a limited number of spots to be measured simultaneously.³² Taken together, FCS-based approaches are essentially limited to dilute samples, put high demands on molecular brightness of the sample, and require a combination of high sensitivity, time resolution, and noise suppression of the detection.

Recently, we presented a concept and its experimental realization which circumvents the above limitations yet maintains the same favorable combination as in FCS of a high detection sensitivity by fluorescence and a strong environmental responsiveness.³³ Applying an excitation source modulated in the range of the relaxation time of the transient state of a fluorescent dye, this state is populated to significantly different degrees depending on the repetition rate and duration of the pulses, provided that the illumination intensity is high enough to drive the fluorophores into this transient state to a significant

degree. The transient state parameters can then be extracted from the systematic variation of the time-averaged fluorescence, reflecting the corresponding population variations of the electronic states induced by changes in the pulse characteristics.

The modulation approach can analyze samples at higher concentrations, where the spontaneous fluorescence fluctuations of individual molecules would tend to average out and which would not be detectable with FCS. Instead, limitations are set by the influence that high concentrations may have on the fluorescence properties of the molecules themselves. Such effects are often observed at concentrations of $10 \mu\text{M}$ or higher.³³ This is typically far beyond the concentration range of FCS and other fluorescence fluctuation techniques. In contrast to FCS, the modulated excitation concept therefore does not rely on a strong fluorescence brightness of the molecules investigated. As previously shown, for the dye Rhodamine 6G in aqueous solution, transient state (TRAST) monitoring by modulated excitation can provide a reliable determination of the triplet-state parameters also when the fluorescence is attenuated by up to 4 orders of magnitude using a neutral density filter.³³ The molecular brightness of the Rh6G molecules after this attenuation is far lower than that of most other fluorophores. Fluorophores with much higher triplet quantum yields than rhodamine dyes ($\sim 1\%$) are thus, from a fluorescence brightness point of view, not a problem but can instead provide higher triplet-state populations and thus a better contrast and sensitivity. The modulation approach is fully compatible with low time resolution detection, for instance, by a CCD camera.³³ The time-modulated excitation experienced by a stationary sample can also be generated by scanning the excitation with respect to the sample, or vice versa. In this way, the excitation need not be idle, and, in particular, for low duty-cycle excitation, a larger sample volume can be interrogated within the same period of time. On the basis of this notion, we recently established the transient state imaging concept by use of a laser scanning confocal microscope (LSCM).³⁴

In this work, we combine the transient state (TRAST) imaging concept above with a time-modulated TIR-based evanescent field excitation. An experimental realization is presented along with the models to interpret the detected steady-state fluorescence data generated by the time-modulated evanescent excitation field. It is shown how the modulation scheme of the excitation can be adapted to cover larger time domains, allowing not only triplet-state dynamics of organic fluorophores to be monitored but also the dynamics and population of their photo-oxidized states. Variation of oxygen concentrations and redox environments were found to be accurately reflected in the measured transient state rate parameters, and images could be generated reflecting both local triplet populations, as well as reduction and oxidation conditions. The presented concept can be expected to offer useful local environmental information close to biological surfaces, that is, with respect to oxidative stress and local oxygen concentrations and turnover.

Theory

Electronic State Model. In this work, we monitor electronic state transitions, based on a model as depicted in Figure 1A comprising the ground and excited singlet states (S_0 and S_1), the lowest triplet state (T_1), and a photo-oxidized state (\dot{R}^+). In the model, k_{exc} represents the excitation rate and k_{10} the deactivation rate of S_1 to S_0 and includes both the rates of fluorescence decay and internal conversion. The rate of inter-system crossing from S_1 to T_1 is denoted by k_{isc} , and k_T is the decay rate of T_1 back to S_0 . The rates of photo-oxidation into

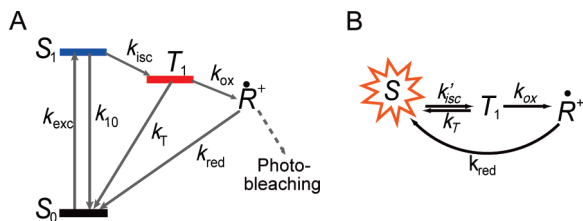


Figure 1. (A) State diagram of a typical organic dye molecule as Rh110, showing the ground singlet state (S_0), the first excited singlet state (S_1), and the lowest triplet state (T_1) and the oxidized radical state (\dot{R}^+). The parameters k_{exc} , k_{10} , k_{isc} , k_T , k_{ox} , and k_{red} are the rate constants for excitation to S_1 , relaxation of S_1 to S_0 , intersystem crossing from S_1 to T_1 , relaxation of T_1 to S_0 , oxidation of T_1 to \dot{R}^+ , and reduction from \dot{R}^+ to S_0 , respectively. (B) Simplified electronic state diagram, focusing on processes orders of magnitude slower than the transitions between the singlet states. The electronic state S represents here the total population in the singlet states, that is, $S = S_0 + S_1$, and k'_{isc} is the effective intersystem crossing rate, given by eq 4.

\dot{R}^+ and the rate of reduction of \dot{R}^+ back into S_0 are denoted by k_{ox} and k_{red} , respectively. The excitation rate, k_{exc} , is given by

$$k_{\text{exc}}(\bar{r}, t) = \sigma_{\text{exc}} I(\bar{r}, t) \quad (1)$$

where σ_{exc} denotes the excitation cross section of the fluorophore and $I(\bar{r}, t)$ is the excitation intensity given by the evanescent field in the TIR arrangement. In cylindrical coordinates $\bar{r} = (r, \varphi, z)$, the excitation intensity can be approximated by a 2D Gaussian distribution in the radial directions and a decaying exponential in the axial z direction²⁷

$$I(\bar{r}, t) = \xi \frac{2I_0}{\pi R^2} \exp\left(-\frac{2r^2}{R^2}\right) \exp\left(-\frac{z}{d_z}\right) P(t) \quad (2)$$

Here, I_0 is the central peak excitation irradiance, R is the $1/e^2$ radius of the Gaussian, and d_z is the $1/e$ decay value of the evanescent field in z , given by $d_z = \lambda/4\pi(n_1^2 \sin^2 \theta - n_2^2)^{-1/2}$, with n_1 and n_2 denoting the indices of refraction of glass and water, respectively, and θ the incident angle of the laser onto the glass surface. $P(t)$ denotes the time dependence of the laser intensity modulation, with $0 \leq P(t) \leq 1, \forall t$. The factor ξ signifies the enhancement factor for the intensity at dielectric surfaces for totally reflected incident beams²⁷

$$\xi = \frac{1}{2} \left(\frac{4 \cos^2 \theta (2 \sin^2 \theta - n^2)}{n^4 \cos^2 \theta - n^2} + \frac{4 \cos^2 \theta}{1 - n^2} \right) \quad (3)$$

where n is the ratio between the refractive indices of water and glass, $n = n_2/n_1$.

The formation of oxidized states as well as photodegradation has been found to increase nonlinearly with the excitation intensity. This has been attributed mainly to formation of higher singlet and triplet states, from which oxidation can occur with a significantly higher probability.²³

The absorption cross sections of S_1 and T_1 into higher singlet and triplet states of xanthene dyes are typically on the order of 10^{-17} cm^2 ,^{6,23} and the decay rates of these higher states typically take place in the range 10^{13} s^{-1} .^{35,36} For the range of excitation intensities applied in this study, higher singlet and triplet states are thus populated to a limited extent and are therefore not included in the model (cf. Figure 1).

The quantum efficiency of triplet-state formation, given by $k_{\text{isc}}/(k_{\text{isc}} + k_{10})$, is relatively low for most organic dyes used in fluorescence spectroscopy (about 0.004 for the rhodamine used in this study). In addition, the lifetime of the triplet state, $1/k_T$, is long (microseconds to milliseconds) compared to the typical lifetime (nanoseconds) of the singlet excited state ($1/k_{10}$).

Consequently, population equilibration between the two singlet states has typically occurred on the time scale of the transitions to and from the triplet states. On the latter time scale, the S_0 and S_1 states can thus be merged into a single state, S , as shown in Figure 1B, with an effective intersystem crossing rate of k'_{isc} from S to T_1 given by^{20,23}

$$k'_{\text{isc}}(\bar{r}, t) = k_{\text{isc}} \frac{k_{\text{exc}}(\bar{r}, t)}{k_{\text{exc}}(\bar{r}, t) + k_{10}} \quad (4)$$

In relation to triplet-state relaxation, formation and decay of the radical state has been found to occur at a yet slower time scale, with typical k_{ox} and k_{red} rates in the ms^{-1} range.²³ Therefore, equilibrium between the singlet and triplet states has typically occurred on the time scale of photo-oxidation. Additionally, as the formation rate of radical states from S_1 differ only by a scaling factor from the radical state formation via T_1 ,²³ we consider here the radical state formation to occur only from T_1 , even though photo-oxidation is believed to occur from both excited singlet and triplet states.

In the model, diffusion of the fluorescent molecules is not explicitly included. However, in particular, for fast diffusing free fluorophores, some influence of diffusion on the analysis can be expected.

For the TIR arrangement in this work, the axial passage times of the freely diffusing fluorophores through the excitation volume were found to be in the microsecond range.²⁵ The time range of the turnover of the long-lived radical state is then typically slower than the diffusion-mediated renewal of fluorophores from the pool of fresh, fluorescently viable fluorophores outside of the excitation volume. In contrast to FCS, which relies on correlated fluorescence photons from single-molecule passage events, TRAST imaging allows molecular processes slower than the passage time of the molecules to be studied. For fast diffusing free fluorophores, however, when applying the model of Figure 1B, diffusional exchange leads to overestimated k_{red} and underestimated k_{ox} rates. Simulations analyzing this influence in further detail are presented in the Results and Discussion section.

Population Dynamics of the Electronic States upon Continuous Constant Excitation. Given the three-state model of Figure 1B, the evolution of the populations S , T_1 , and \dot{R}^+ of a fluorophore, located at a point \bar{r} at a time t after the onset of excitation ($P(t) = 1 \forall t \geq 0$) can be described by the following system of coupled first-order differential equations

$$\begin{aligned} \frac{d}{dt} \begin{pmatrix} S(\bar{r}, t) \\ T_1(\bar{r}, t) \\ \dot{R}^+(\bar{r}, t) \end{pmatrix} &= \begin{bmatrix} -k'_{\text{isc}}(\bar{r}, t) & k_T & k_{\text{red}} \\ k'_{\text{isc}}(\bar{r}, t) & -(k_{\text{ox}} + k_T) & 0 \\ 0 & k_{\text{ox}} & -k_{\text{red}} \end{bmatrix} \begin{pmatrix} S(\bar{r}, t) \\ T_1(\bar{r}, t) \\ \dot{R}^+(\bar{r}, t) \end{pmatrix} \\ &= \mathbf{M} \begin{pmatrix} S(\bar{r}, t) \\ T_1(\bar{r}, t) \\ \dot{R}^+(\bar{r}, t) \end{pmatrix} \end{aligned} \quad (5)$$

with the coupling matrix of the system hereafter referred to as \mathbf{M} .

As shown earlier,^{20,33} the evolution of the three states upon continuous constant excitation can be derived using the eigenvalues and eigenvectors of the matrix, \mathbf{M} , in eq 5. Regarding the populations as probabilities, $([S(\bar{r}, t) + T(\bar{r}, t) + R(\bar{r}, t)] = 1)$, and assuming a completely relaxed system at $t = 0$ yields the initial condition

$$\begin{aligned} S(\bar{r}, 0) &= 1 \\ T_1(\bar{r}, 0) &= 0 \\ \dot{R}^+(\bar{r}, 0) &= 0 \end{aligned} \quad (6)$$

Solving eqs 5 and 6 and assuming the triplet-state kinetics to be much faster than the radical state kinetics yields the following evolution of the singlet state's population

$$\begin{aligned} S(\bar{r}, t) = & \frac{k_{\text{red}} k_T}{k'_{\text{isc}}(\bar{r})(k_{\text{ox}} + k_{\text{red}}) + k_{\text{red}} k_T} \exp(\lambda_1(\bar{r})t) + \\ & \frac{k'_{\text{isc}}(\bar{r})}{k'_{\text{isc}}(\bar{r}) + k_T} \exp(\lambda_2(\bar{r})t) + \\ & \frac{k'_{\text{isc}}(\bar{r}) k_T k_{\text{ox}}}{(k'_{\text{isc}}(\bar{r}) + k_T)[k'_{\text{isc}}(\bar{r})(k_{\text{ox}} + k_{\text{red}}) + k_T k_{\text{red}}]} \exp(\lambda_3(\bar{r})t) \end{aligned} \quad (7)$$

where the eigenvalues λ_1 , λ_2 , and λ_3 of the coupling matrix \mathbf{M} of eq 5 are approximated by

$$\begin{aligned} \lambda_1(\bar{r}) &= 0 \\ \lambda_2(\bar{r}) &\approx -k'_{\text{isc}}(\bar{r}) - k_T = -k_{\text{isc}}(\bar{r}) \frac{k_{\text{exc}}(\bar{r}, t)}{k_{\text{exc}}(\bar{r}, t) + k_{10}} - k_T \\ \lambda_3(\bar{r}) &\approx -k_{\text{ox}} \frac{k'_{\text{isc}}(\bar{r})}{k'_{\text{isc}}(\bar{r}) + k_T} - k_{\text{red}} \end{aligned} \quad (8)$$

The first eigenvalue, λ_1 , is 0, indicating that the populations in the three states, as a closed system, will approach a steady state as $t \rightarrow \infty$. The magnitude of the second eigenvalue is related to the rate at which the triplet state is built up, and its inverse absolute value corresponds to the triplet-state relaxation time. The magnitude of the third eigenvalue describes the buildup rate of the radical state.

Average Fluorescence Response to a Low Duty Cycle Excitation Pulse Train. The emitted fluorescence, $F(\bar{r}, t)$, from a fluorophore with fluorescence quantum yield Φ_f located at position \bar{r} is proportional to the probability, $S_1(\bar{r}, t)$, that the excited singlet state of the fluorophore is occupied at time t

$$F(\bar{r}, t) = \Phi_f k_{10} S_1(\bar{r}, t) = \Phi_f k_{10} \frac{k_{\text{exc}}(\bar{r}, t)}{k_{\text{exc}}(\bar{r}, t) + k_{10}} S(\bar{r}, t) \quad (9)$$

Applying to the sample a square-wave excitation pulse train, with N pulses of duration w and period T , the total detected time-averaged fluorescence, \bar{F} , will reflect the average S_1 population probability of the fluorescent molecules in the detection volume. In general, when calculating \bar{F} , the population dynamics of S_1 have to be considered both when the excitation is active and when it is idle in between the pulses.³³ However, for the low duty cycle ($\eta = w/T \leq 1\%$) pulse trains used in this work, the fluorophores can be considered to be totally relaxed to the singlet ground state at the onset of every new pulse (Supporting Information, Figure S1). The average fluorescence response to a train of N excitation pulses of width w can then be approximated by

$$\bar{F}(w) = \frac{1}{NT} \iiint \Phi_D \Gamma(z) k_{10} \Phi_f \sum_{i=0}^{N-1} \left(\int_{iT}^{iT+w} c(\bar{r}, t) \frac{k_{\text{exc}}(\bar{r}, t)}{k_{10} + k_{\text{exc}}(\bar{r}, t)} S(\bar{r}, t) dt \right) dV \quad (10)$$

Here, NT is the total duration of the excitation pulse train, and Φ_D denotes the quantum efficiency of the detector. Fur-

thermore, the anisotropic fluorescence emission close to a dielectric surface is accounted for by the fraction of power, $\Gamma(z)$, emitted by a fluorophore at distance z from the interface into the cone of light accepted by the objective. This parameter $\Gamma(z)$ results in additional weighting of fluorophores close to the interface and was approximated in this study by a single exponential.^{25,37} Due to the low duty cycle of excitation, any changes in the concentration of fluorescent molecules, $c(\bar{r}, t)$, attributed to photodegradation can be kept quite low and are otherwise eliminated from the analysis by regular calibration recordings (see the Materials and Methods section).

On the basis of a 2D Gaussian distribution of the excitation intensity in the radial plane, as given by eq 2, the overall excitation volume can be divided into radial increments within which the excitation intensity can be considered nearly equal in the radial dimension.

Within each radial shell ($r, r + dr$) the average (in time and space) fluorescence intensity response to different pulse trains is given by

$$\bar{F}(w, r) = \frac{1}{NT2\pi r dr} \int \left[\int_0^{2\pi} \int_r^{r+dr} \Phi_D \Gamma(z) k_{10} \Phi_f \sum_{i=0}^{N-1} \left(\int_0^w c(\bar{r}, t) \frac{k_{\text{exc}}(\bar{r}, t)}{k_{10} + k_{\text{exc}}(\bar{r}, t)} S(\bar{r}, t) dt \right) r dr d\varphi \right] dz \quad (11)$$

The average fluorescence intensity within one excitation pulse of duration w and from a fluorescent molecule located within a distance r to $(r + dr)$ from the center of the excitation field is obtained by dividing the average detected fluorescence by the duty cycle, $\eta = w/T$, of the excitation pulse train

$$\bar{F}_{\text{exc}}(w, r) = \bar{F}(w, r)/\eta \quad (12)$$

If $\bar{F}_{\text{exc}}(w, r)$ is normalized to 1 for $w \ll 1/\lambda_2$, it represents the time-averaged population of the two singlet states (eq 7) in the corresponding radial region and within the duration of the excitation pulse, denoted as $\langle S(w, r) \rangle_w$, and is given by

$$\langle S(w, r) \rangle_w = \frac{\bar{F}_{\text{exc}}(w, r)}{(\bar{F}_{\text{exc}}(w, r))|_{w \ll \lambda_2}} = \int \left(\int_0^w S(t, r) dt \right) dz \quad (13)$$

Materials and Methods

Instrumental Setup. The instrumentation used in this study is based on a previously described setup for TIR-FCS,³⁸ to which an acousto-optical modulator (AOM) has been added for excitation intensity modulation. The principle of the modulated excitation TIR microscope is shown in Figure 2. Briefly, a single-line 491 nm diode laser (Calypso, Cobolt AB, 15–75 mW) is first passed through an AOM (MQ 180-AO, 25-VIS, AA OptoElectronic) and then a neutral density filter to fine-adjust excitation power. The intensity modulated laser beam is made circularly polarized using a $\lambda/4$ wave plate (Optosigma) and focused at the back focal plane of an oil immersion objective (alpha-Plan-Fluar, 100 \times , NA 1.45, Carl Zeiss).

The dichroic mirror (F500-Di01, Semrock Inc.) mounted together with the focusing lens on a linear translator is used to introduce a fixed beam offset of more than 2.2 mm from the optical axis. The resulting incident angle, θ , is estimated to 63.7°. The radial extension of the excitation is estimated to 18 μm in diameter at the glass/water interface ($1/e^2$ value), as described in the data analysis. About 42% of the laser power (~31.5 mW for a laser output power of 75 mW) is delivered to the interface, as measured by a power meter (PM100, Thorlabs).

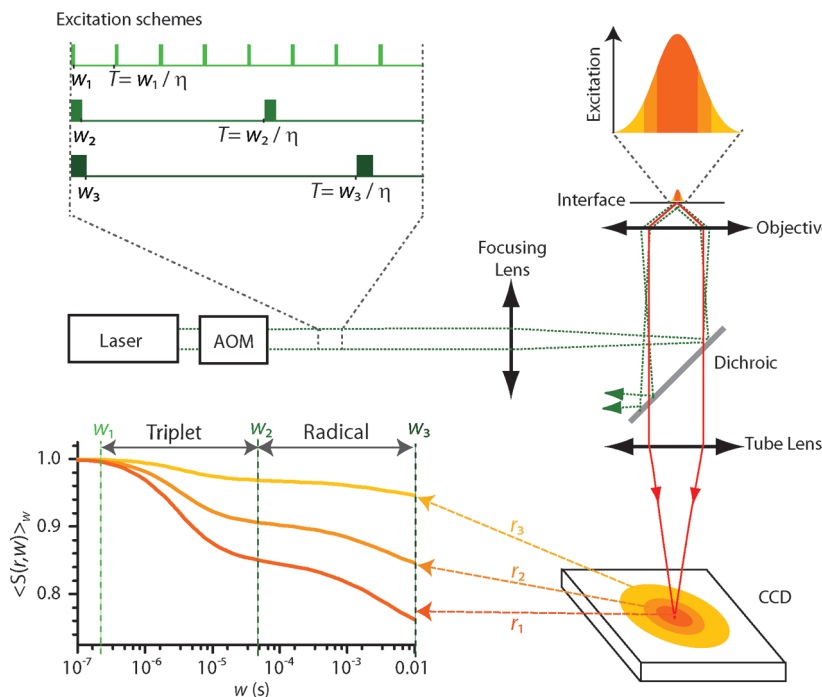


Figure 2. Setup and measurement principle. The green dashed lines show the laser excitation pathway through the AOM, yielding pulse trains with increasing pulse widths but constant duty cycle, η , as shown in the upper left inset. The pulsed laser excitation is focused off axis on the back focal plane of the objective. At the dielectric interface, an evanescent excitation field is generated, exponentially decaying in the axial direction and forming a 2D Gaussian in the radial dimension. The image of the fluorescence generated by this excitation field is divided into regions of similar excitation intensities, as shown on the CCD. For simplicity, only three regions have been represented; in reality, the Gaussian is divided into 30 regions. The averaged and normalized response curves of each region, $\langle S(w,r) \rangle_w$, are shown on the lower left inset. Two processes are schematized on this plot, one related to the triplet state, T_1 , and a second one related to the radical state, \dot{R}^+ .

The emitted fluorescence is collected with the same high-NA objective and focused with an achromatic tube lens onto either an electron multiplying CCD (Luca, Andor Technology, used in quarter screen mode, 330×248 pixels) for TRAST imaging measurements or two $50 \mu\text{m}$ multimode fibers (FiberTech, Berlin, Germany), each connected to an avalanche photodiode (SPCM-AQR-14-FC, Perkin-Elmer Optoelectronics) for FCS measurements. A flip mirror is used to switch between the FCS and CCD imaging modes. FCS is mainly used for controlling the focus position to the glass/water interface using a piezo stage (Nanomax TS, Thorlabs).

A Graphical User Interface is programmed in Matlab to control the acquisition hardware. The camera is controlled in Matlab via USB using a driver based on the MCD Software Development Kit from Andor Technology. The diode laser is controlled via a home-built Serial Port driver and the Piezo controller via an ActiveX driver. The modulation scheme of the AOM is set via a National Instruments PCI 6602 card connected to the modulator controller (AA.Mod.XX, AA Opto Electronic).

Measurement Protocol. A typical TIR-TRAST measurement consists of a series of 30 images acquired at different pulse widths of the modulated excitation, distributed logarithmically between 100 ns and 10 ms. As shown in the upper-left part of Figure 2, for each pulse scheme, the pulse period is increased by the same factor as the pulse width, w , in order to keep the duty cycle constant throughout the measurement (typically $\eta \leq 1\%$). Additionally, for each pulse scheme, the number of pulses is adapted in order to keep the total illumination time constant. Typically, an illumination time of 100 ms is chosen, yielding at a 1% duty cycle a CCD camera exposure time of 10 s per image.

Intermittently, before every fifth image, a control image is recorded at the shortest pulse width to visualize drifts in

fluorescence caused by measurement artifacts related to concentration or focus position changes. To minimize drift in the focal height, the position of the fluorescent spot on the CCD image is monitored before each new pulse train in order to keep the excitation focused on the glass/water interface by feedback control of the piezo stage.

The nonzero extinction factor of the AOM (approximately 0.1%) is accounted for by subtracting an image recorded with an undeflected AOM beam from the other images. The temporal shape of the AOM excitation pulses is calibrated by a time-resolved measurement of the scattered light from a pure water sample as described previously.³³

Data Analysis. The radial extension of the excitation profile was obtained by fitting the fluorescence image at the shortest excitation pulse width (100 ns) to a 2D Gaussian distribution. At this pulse width, the excitation profile is essentially free from fluorescence saturation effects due to triplet and radical state formation. Also, singlet-state saturation can be neglected because of the moderate excitation rates (maximum $k_{\text{exc}} \approx 60 \mu\text{s}^{-1} \ll k_{10}$). Additional deviations from a Gaussian shape due to TIR beam shape artifacts as forward scattering were small and could be neglected.

As described in eq 11, the data acquired by the CCD camera was collected in 30 radial shells exposed to nearly equal excitation intensities. For each radial region, the excitation was assumed constant in the radial direction, whereas the exponentially decaying excitation intensity in the axial direction z of eq 2 was accounted for by subdividing each region into 50 z domains. The local excitation rate was calculated according to eq 2 and from the measured power at the dielectric interface. The optical parameters of the TIR excitation and the photochemical parameters used in the data analysis are summarized in Table 1.

TABLE 1: Assumed Parameters for the Data Analysis and Simulation

λ	wavelength	491 nm
n_1	refractive index of glass	1.52
n_2	refractive index of water	1.33
θ	TIR incident angle	63.7°
σ	fluorophore excitation cross section (@ 491 nm) ²⁷	$2.50 \times 10^{-16} \text{ cm}^2$
k_{10}	fluorescence decay rate ²⁷ (including internal conversion)	$244 \times 10^6 \text{ s}^{-1}$

The fluorescent responses of each of the radial regions were simultaneously fitted according to eq 11 and 12 using a Levenberg–Marquardt algorithm in Matlab 7.7 (The Mathworks, Inc., U.S.A.). Weights accounting for the Poissonian statistics of the fluorescence signal were estimated by the standard variation of the fluorescence, $\sigma_r(w)$, within the N_r pixels of each region ($r, r + dr$) and applied to each radial region

$$\omega_r(w) = \frac{\sqrt{N_r}}{\sigma_r(w)} \quad (14)$$

In the fitting process, k_{isc} , k_T , and k_{red} were extracted as global parameters, while k_{ox} was allowed to vary within the excitation volume, as explained in the Results and Discussion section. The confidence intervals of the fitting parameters referred to in this work were calculated by error propagation, including the 95% confidence interval of the fit and uncertainties in the measurement parameters (laser power, diameter of the excitation, incident angle of the excitation beam, and pulse width correction). In a last step, the fluorescent responses of the radial shells were normalized to 1 as described in eq 13, yielding $\langle S(w,r) \rangle_w$ (cf. lower-left inset of Figure 2).

Surface Preparation. The glass microscope coverslips (no. 1, diameter = 25 mm, Hecht Assistent, Germany) were cleaned according to the protocol described previously.²⁷ Three consecutive ultrasonic baths in Helmanex (2%), acetone/ethanol (30/70%), and ultrapure water were alternated with thorough rinsing with ultrapure water. The cover glasses were then rinsed with spectroscopically pure ethanol, blown dry with nitrogen flow, plasma etched for 2 min in a reactive ion etcher (PlasmaLab 80 Plus, Oxford Instrument, United Kingdom), and finally stored in PBS. Prior to measurements, the cover glasses were rinsed in ultrapure water and blown dry by nitrogen.

Fluorophores and Chemicals. Rhodamine 110 (Rh110, Sigma Chemicals, St. Louis, U.S.A.) prepared as an ethanol stock solution was diluted in PBS buffer to about 40 nM concentration prior to the measurements. PBS (pH 7.4, 150 mM salt concentration) buffer was prepared from salts of analytical grade. High salt concentrations were used to minimize electrostatic interactions between the surface and the zwitterionic Rh110 fluorophores.²⁷

Stock solutions of ascorbic acid (Sigma Chemicals, St. Louis, U.S.A.) were freshly prepared in nanopure water and then diluted in the fluorophore PBS buffer solutions prior to measurements.

Control of the Dissolved Oxygen Concentration in Solution. Different oxygen–argon gas mixtures were bubbled into water in a sealed container with an incorporated oxygen sensor (Inlab 605 O₂ sensor, Mettler Toledo). The sensor was calibrated with respect to two calibration points using the atmospheric oxygen content in the air and Zero Oxygen Standard Tablets (Metler Toledo). After measuring the dissolved oxygen content, the humidified gas mixture was flowed through a sealed chamber containing the 100 μL sample droplet. Equilibration was found to have occurred after 10 min.

TABLE 2: Parameters Assumed Only for the Simulation

P_L	laser power at the interface	31.5 mW
R	radius of gaussian excitation	10 μm
k_{isc}	intersystem crossing rate ²⁷	$1 \times 10^6 \text{ s}^{-1}$
k_T	triplet relaxation rate ²⁷	$0.45 \times 10^6 \text{ s}^{-1}$
k_{ox}	oxidation rate	2000 s^{-1}
k_{red}	reduction rate	100 s^{-1}
D	diffusion coefficient	$4.1 \times 10^{-6} \text{ cm}^2 \text{ s}^{-1}$, $4.1 \times 10^{-8} \text{ cm}^2 \text{ s}^{-1}$ ⁴⁰

Computer Simulations. To simulate the triplet and radical population buildup upon laser excitation, finite element analysis was performed using a commercial finite element analysis software (Multiphysics, COMSOL AB, Stockholm, Sweden). Due to the symmetry of the evanescent excitation field, a 2D model in $\bar{r} = (r, z)$ was chosen, where three species of the Rh110 fluorophores (singlet state, triplet state, and radical), subject to the differential equations of eq 5, were allowed to diffuse according to the diffusion equation

$$\frac{\partial}{\partial t} \begin{pmatrix} S(\bar{r}, t) \\ T_1(\bar{r}, t) \\ \dot{R}^+(\bar{r}, t) \end{pmatrix} = D \nabla \begin{pmatrix} S(\bar{r}, t) \\ T_1(\bar{r}, t) \\ \dot{R}^+(\bar{r}, t) \end{pmatrix} + \mathbf{M} \begin{pmatrix} S(\bar{r}, t) \\ T_1(\bar{r}, t) \\ \dot{R}^+(\bar{r}, t) \end{pmatrix} \quad (15)$$

The excitation is assumed to be distributed spatially according to eqs 1 and 2 and initiated at time $t = 0$ with a duration of w . To simulate the emitted fluorescence acquired by the CCD camera, the excited singlet population was integrated over different radial shells according to eqs 11–13. The parameters used in the simulation are summarized in Tables 1 and 2.

Results and Discussion

A series of TIR-TRAST measurements were performed on Rh110 in PBS solution using a wide range of pulse widths, w , as described above. With increasing w , the averaged and normalized fluorescence response, yielding $\langle S(w,r) \rangle_w$, was found to drop in two major steps on a logarithmic time scale, as shown in Figure 3A. The first decay step had a characteristic time in the microsecond time range, and the second decay took place on the order of milliseconds. Curves from different radial shell regions were fitted globally, as described above. The fitted curves are included in Figure 3A and show a good agreement to the experimental data. This suggests that the first decay found on the microsecond time scale is attributed to the triplet-state properties of the fluorophore, whereas the second decay in the millisecond time range is a result of electron transfer (oxidation–reduction) of the fluorophores.

All fitting parameters except the oxidation rate, k_{ox} , were found to be independent of the excitation intensity and could be fitted globally, that is, single k_{isc} , k_T , and k_{red} rates were sufficient to describe the fluorescence response within all of the radial shells to the different intensities of the modulated excitation. The excitation intensity dependence of k_{ox} can be related to the formation of singlet oxygen molecules and other reactive oxygen species, formed in particular when triplet-state fluorophores are quenched by molecular oxygen. Singlet oxygen has a lifetime in aqueous solution of approximately 3 μs, is highly reactive, and can readily undergo oxidation reactions with neighboring species.³⁹ A larger net exchange of both photo-oxidized fluorophores and singlet oxygen molecules with the bulk volume can be expected in the peripheral parts of the excitation volume, resulting in spatial concentration gradients of these species. Since the spatial distribution of their generation rates also largely correlates with the excitation intensity distribution, a spatial dependence of the k_{ox} rate can appear. Under air-

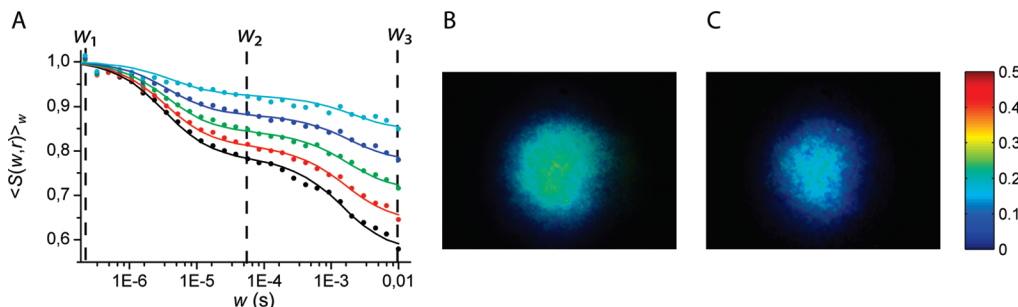


Figure 3. (A) Measured normalized average fluorescence, $\langle S(w,r) \rangle_w$, of Rh110 in an air-equilibrated PBS solution versus the excitation pulse width w for five (out of in total 30) representative radial shell regions experiencing different excitation intensities (filled circles). Parameter fitting of the data from all 30 shell regions to eqs 11 and 12 yields $k_{\text{isc}} = 1.2 \pm 0.2 \mu\text{s}^{-1}$, $k_T = 0.37 \pm 0.02 \mu\text{s}^{-1}$, $k_{\text{ox}} = 1.5 \pm 0.1 \text{ ms}^{-1}$, and $k_{\text{red}} = 0.78 \pm 0.05 \text{ ms}^{-1}$. Solid lines show the resulting $\langle S(w,r) \rangle_w$ versus w for the five radial shell regions. (B, C) T_1 and R^+ images, generated by use of eqs 16 and 17, respectively, and from images recorded at the pulse widths w_1 , w_2 , and w_3 , as indicated in Figure 3A. The color scales (right) indicate the average relative population level of the T_1 and R^+ states during active excitation.

equilibrated conditions, we observe a variation of k_{ox} from 0.8 up to 1.5 ms^{-1} , as measured in the most peripheral and in the central radial region, respectively. In the following, only the maximum k_{ox} rate, measured in the central radial shell, is stated.

The fit, performed as described above, yielded triplet-state parameters of $k_{\text{isc}} = 1.2 \pm 0.2 \mu\text{s}^{-1}$ and $k_T = 0.37 \pm 0.02 \mu\text{s}^{-1}$, and redox rate parameters of $k_{\text{ox}} = 1.5 \pm 0.1 \text{ ms}^{-1}$ and $k_{\text{red}} = 0.78 \pm 0.05 \text{ ms}^{-1}$. The triplet-state parameter values show a relatively good agreement with the corresponding parameters of Rh110 determined by confocal FCS ($k_{\text{isc}} = 1 \mu\text{s}^{-1}$ and $k_T = 0.45 \mu\text{s}^{-1}$) and by TIR-FCS ($k_{\text{isc}} = 1.3 \mu\text{s}^{-1}$ and $k_T = 0.49 \mu\text{s}^{-1}$).²⁷ These latter results were also validated by TIR-FCS measurements performed under the same conditions as the TIR-TRAST measurements in this work (data not shown). The electron-transfer rates obtained can be compared to those derived by FCS measurements for the dye Rhodamine 6G (Rh6G) in aqueous solution and with micromolar concentrations of a reducing agent (*n*-propyl gallate) ($k_{\text{ox}} = 4 \text{ ms}^{-1}$ and $k_{\text{red}} = 0.2 \text{ ms}^{-1}$).²³ In the absence of a reducing agent, the reduction and oxidation rates cannot so easily be analyzed by conventional FCS measurements. Their relaxation times are then typically too slow to occur within the dwell times of the molecules in the FCS detection volume, which defines the observation time window.²³

The difference between the redox rates determined here for the dye Rh110 and those determined by FCS for Rh6G can be due to the different hydrophobic and redox properties of the dyes. A second major reason for the difference is that in our measurements, the redox rates may be influenced by diffusion-mediated renewal of fluorophores. This effect was further analyzed by simulations, as described below.

From the fluorescence data, population images of the triplet and of the photo-oxidized states could be generated (Figure 3B and C, respectively). These, so-called T_1 and R^+ images were calculated pixel-wise by image-ratioing, by dividing the time-averaged fluorescence intensity within the excitation pulse, for pulse widths much longer and shorter than the triplet relaxation time ($1/\lambda_2$) and the time of build-up of the radical state ($1/\lambda_3$), respectively.

$$T_1(\bar{r}) = \frac{\bar{F}_{\text{exc}}(w_1, \bar{r}) - \bar{F}_{\text{exc}}(w_2, \bar{r})}{\bar{F}_{\text{exc}}(w_1, \bar{r})_w} \quad (16)$$

$$R^+(\bar{r}) = \frac{\bar{F}_{\text{exc}}(w_2, \bar{r}) - \bar{F}_{\text{exc}}(w_3, \bar{r})}{\bar{F}_{\text{exc}}(w_1, \bar{r})_w} \quad (17)$$

Here, w_i , $i = 1, 2, 3$, represent different excitation pulse widths, with $w_1 \ll 1/\lambda_2$, $1/\lambda_2 \ll w_2 \ll 1/\lambda_3$, and $w_3 \gg 1/\lambda_3$. These

pulse widths can be selected from the fluorescence response curves, as indicated in Figure 3A.

Simulation. To investigate how the measured kinetic rates, especially the redox rates, are influenced by the renewal of fluorophores diffusing into and out of the detection volume, simulations were performed as described in the Materials and Methods section and with parameter values as given in Tables 1 and 2.

Figure 4A–C shows the resulting electronic state populations of the fluorophores along the z direction at the center of the Gaussian excitation profile. The molecular diffusion of the fluorophore molecules has been set to $D = 4.1 \times 10^{-6} \text{ cm}^2 \text{ s}^{-1}$ for this first part of the simulations.⁴⁰ The depletion of S was found to occur in two phases. First, the triplet state, T_1 , became populated in the microsecond range, as shown on Figure 4B. Then, after $100 \mu\text{s}$, the population of the radical state, R^+ , was gradually built up deep into the sample, as shown on Figure 4C. It can be noted that the triplet-state population remains confined to the axial extension of the excitation field, whereas the radical state depletion of the singlet population extends over several micrometers, much beyond the extension of the TIR excitation volume.

The proposed method thus enables photoinduced transient processes to be followed up to the millisecond time range. This is in contrast to FCS, where one measures the probability of detecting a fluorescence photon of a molecule at a time τ after detecting a previous photon originating from the same molecule. In TIR-FCS measurements, the dwell time of the molecules in the detection volume is set by the axial passage times of the fluorophores through the TIR excitation. These times thus limit the time window within which transient state relaxation processes can be observed and are on the order of a few microseconds for freely diffusing fluorophores.^{25,27,41}

In contrast, transient state monitoring by modulated excitation monitors the overall depletion of fluorescence due to transient state buildup in the detection volume following onset of excitation. It does not matter if the fluorescence originates from specific molecules residing in the detection volume during the full excitation period or from molecules entering for the first time or re-entering the excitation volume. Therefore, with the presented method, based on excitation synchronization of the fluorescent molecules rather than the monitoring of their spontaneous blinking behavior, there is no limitation in the observation time window set by the molecular passage times as there would be for FCS measurements.

Figure 5A shows the simulated fluorescence response curves of Rh110 in aqueous solution, as acquired in different radial shells by the CCD camera in a TIR-TRAST measurement. Also

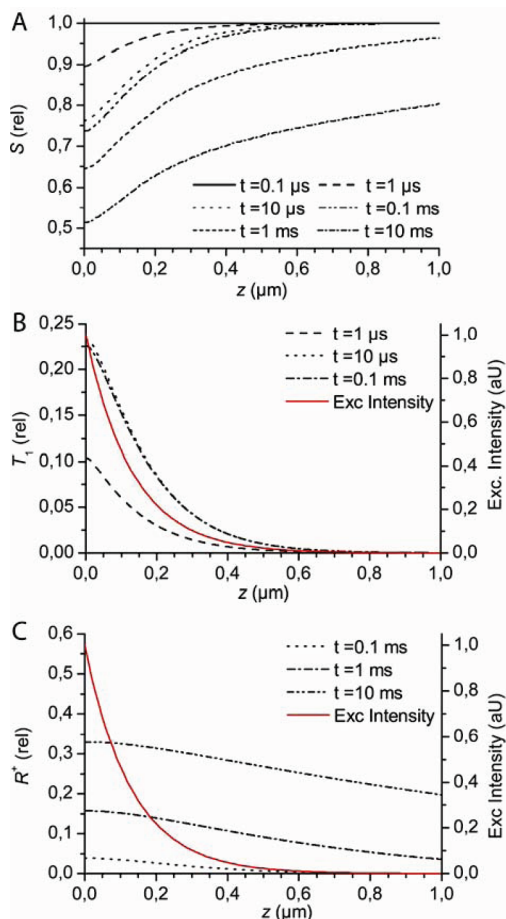


Figure 4. Simulation of the response of the three fluorophore states (S , T_1 , and R^+ , varying according to eq 16), at different moments after the onset of the excitation, as described in eq 2. The graphs show a cross section along z at the center of the excitation. Panel (B) shows that the triplet state reaches its “equilibrium” after about $10 \mu\text{s}$, whereas (C) shows that the radical state, R^+ , is not significantly populated until after $100 \mu\text{s}$. On the latter two figures, the excitation intensity of the evanescent field has been plotted for comparison.

shown are the corresponding simulated curves from a less mobile but otherwise identical fluorescent sample ($D = 4.1 \times 10^{-8} \text{ cm}^2 \text{ s}^{-1}$, Figure 5B). A visual comparison of the two sets of curves indicates that the diffusion influences the relaxation behavior of the response curves attributed to the redox process, while the influence on the measured triplet relaxation seems negligible.

This is also confirmed by global fits of the simulated data as described above. In the simulations, the photophysical parameters were set to $k_{\text{isc}} = 1 \mu\text{s}^{-1}$, $k_T = 0.45 \mu\text{s}^{-1}$, $k_{\text{ox}} = 2 \text{ ms}^{-1}$, and $k_{\text{red}} = 0.1 \text{ ms}^{-1}$. The fit yielded quite accurate triplet parameters in both cases, $k_{\text{isc}} = 0.93 \mu\text{s}^{-1}$ and $k_T = 0.38 \mu\text{s}^{-1}$ for the Rh110 diffusion and $k_{\text{isc}} = 1 \mu\text{s}^{-1}$ and $k_T = 0.42 \mu\text{s}^{-1}$ for the slower diffusion. For the redox rate parameters, the fit yielded $k_{\text{ox}} = 1.1 \text{ ms}^{-1}$ and $k_{\text{red}} = 0.50 \text{ ms}^{-1}$ for Rh110 and $k_{\text{ox}} = 2.5 \text{ ms}^{-1}$ and $k_{\text{red}} = 0.14 \text{ ms}^{-1}$ for the more slowly diffusing species.

For fast, freely diffusing dyes, the used model neglecting the diffusion will thus distort the estimated redox properties of the dye, such that k_{ox} is somewhat underestimated and k_{red} is overestimated. However, although the analysis does not provide accurate absolute values of the redox rates for fast diffusing species, simulations show that relative changes are still well-reflected (cf. Supporting Information). Moreover, if the redox

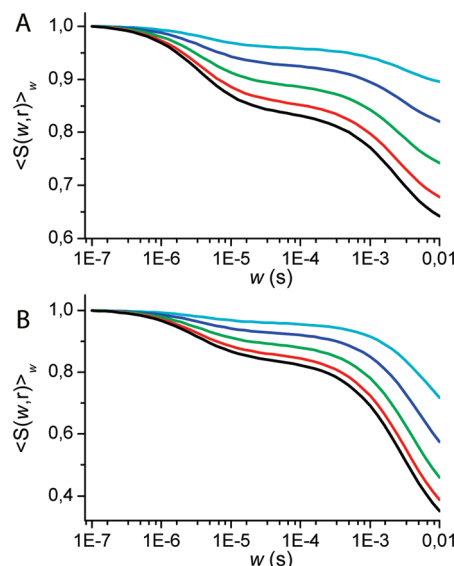


Figure 5. Normalized fluorescence response to a single excitation pulse as a function of the pulse width; simulation for Rh110 in TIR-TRAST measurements using multiphysics finite element simulation software. Triplet kinetic rates and oxidation rates were set according to Table 2. (A) Diffusion coefficient of $D = 4.1 \times 10^{-6} \text{ cm}^2 \text{ s}^{-1}$, comparable to that of Rh110. Fitting of the simulated data to eqs 11 and 12 yields a k_{red} rate overestimated by a factor of 5 and a k_{ox} rate underestimated by a factor 2. (B) Diffusion coefficient of $D = 4.1 \times 10^{-8} \text{ cm}^2 \text{ s}^{-1}$. The radical state population is drastically increased compared to A. Fitting of the simulated data to eqs 11 and 12 here only results in an overestimation of the k_{red} and k_{ox} by 36 and 20%, respectively.

properties are known, the measured relaxation behavior can then possibly also be used to monitor the mobility of the fluorescent species. For more slowly diffusing species, similar to those of large or membrane-bound proteins, the proposed model seems to provide an accurate estimate of the redox rates.

Influence of Molecular Oxygen. Oxygen is well-known to influence the triplet-state kinetics of many fluorophores through spin-orbital coupling and triplet-triplet quenching reactions.^{20,42} The ability of the presented method to monitor changes in the triplet state was investigated by varying the dissolved oxygen concentration [O_2]. In Figures 3 and 6, $\langle S(w,r) \rangle_w$ curves from Rh110 in a PBS buffer solution measurement are shown, recorded under air (Figure 3), pure argon (Figure 6A), and pure oxygen atmospheres (Figure 6C). The oxygen influence is clearly visible by direct visual comparison of the different sets of curves. At very low oxygen concentrations, the amplitude of the triplet-state decay is strongly increased, and its relaxation is shifted to longer times. During long pulse widths ($w > 1/\lambda_2$), no more than 10% of the average fluorescence intensity recorded under short pulse widths ($w \ll 1/\lambda_2$) is left. Following the decay due to triplet-state buildup, no additional decay in the curves can be observed at still longer pulse widths.

Therefore, under argon atmosphere, the curves measured (Figure 6A) do not allow all of the rate parameters to be extracted from the curve fitting. In the fitting procedure, the reduction rates were therefore fixed to $k_{\text{red}} = 0.65 \text{ ms}^{-1}$. This is the mean value of the fitted reduction rates at the other oxygen concentrations (cf. Figure 7D). The fit of the triplet-state parameters to the data in Figure 6A yielded $k_{\text{isc}} = 0.64 \pm 0.08 \mu\text{s}^{-1}$ and $k_T = 6.4 \pm 0.4 \text{ ms}^{-1}$. The significant decrease in k_T by more than an order of magnitude upon oxygen removal confirms that k_T is mainly driven by oxygen quenching, whereas the relative influence of oxygen on k_{isc} is minor. The prominent triplet-state population at deoxygenation is also seen in the corresponding T_1 images, calculated from eq 16 (Figure 6B).

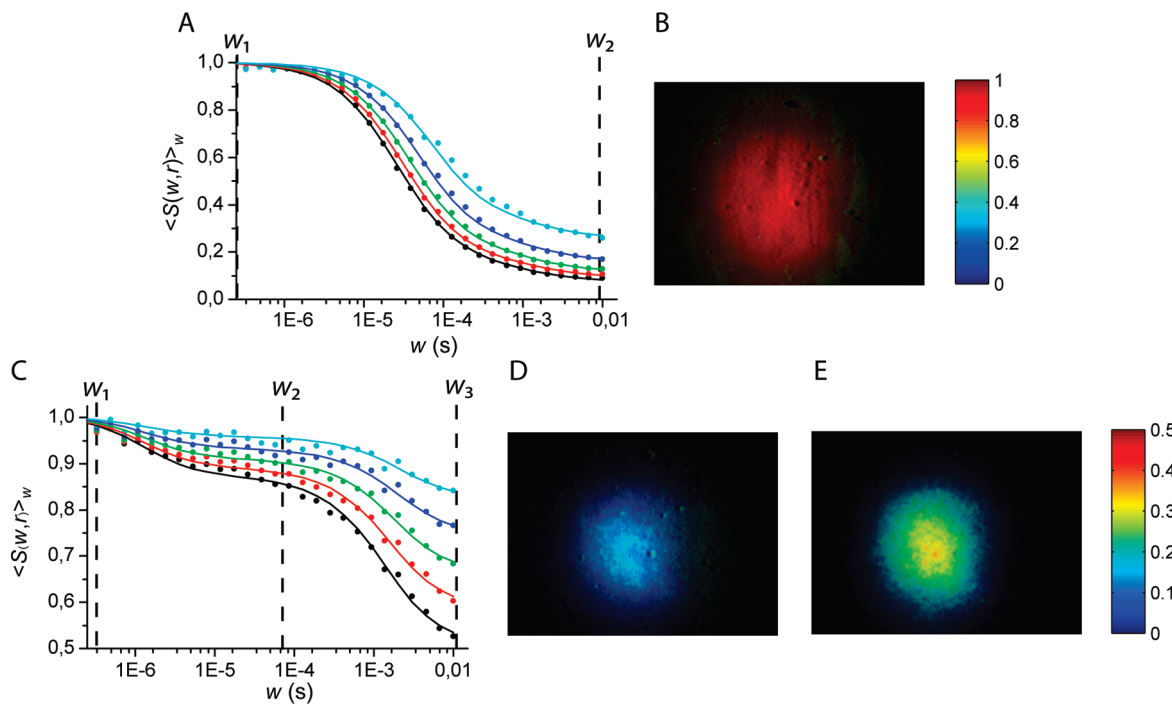


Figure 6. (A) Measured normalized average fluorescence, $\langle S(w,r) \rangle_w$, and fitting results for a Rh110 solution in a pure argon atmosphere. Fitting to eqs 11 and 12 yielded $k_{\text{isc}} = 0.64 \pm 0.08 \mu\text{s}^{-1}$, $k_T = 6.4 \pm 0.4 \text{ ms}^{-1}$, and $k_{\text{ox}} = 0.81 \pm 0.17 \text{ ms}^{-1}$, with the reduction rate fixed to $k_{\text{red}} = 0.65 \text{ ms}^{-1}$. (B) T₁ image, generated as in Figure 3B. (R^+ images could not be extracted from measurement in pure argon atmospheres.) (C) $\langle S(w,r) \rangle_w$ and corresponding fitted curves for a Rh110 solution in a pure oxygen atmosphere. Fitting parameters: $k_{\text{isc}} = 1.8 \pm 0.3 \mu\text{s}^{-1}$, $k_T = 1.1 \pm 0.1 \mu\text{s}^{-1}$, $k_{\text{ox}} = 4.4 \pm 0.2 \text{ ms}^{-1}$, and $k_{\text{red}} = 0.66 \pm 0.03 \text{ ms}^{-1}$. (D) and (E) Corresponding T₁ and R^+ images, generated as in Figure 3B and C. The color scales in (B), (D), and (E) denote average relative populations during active excitation.

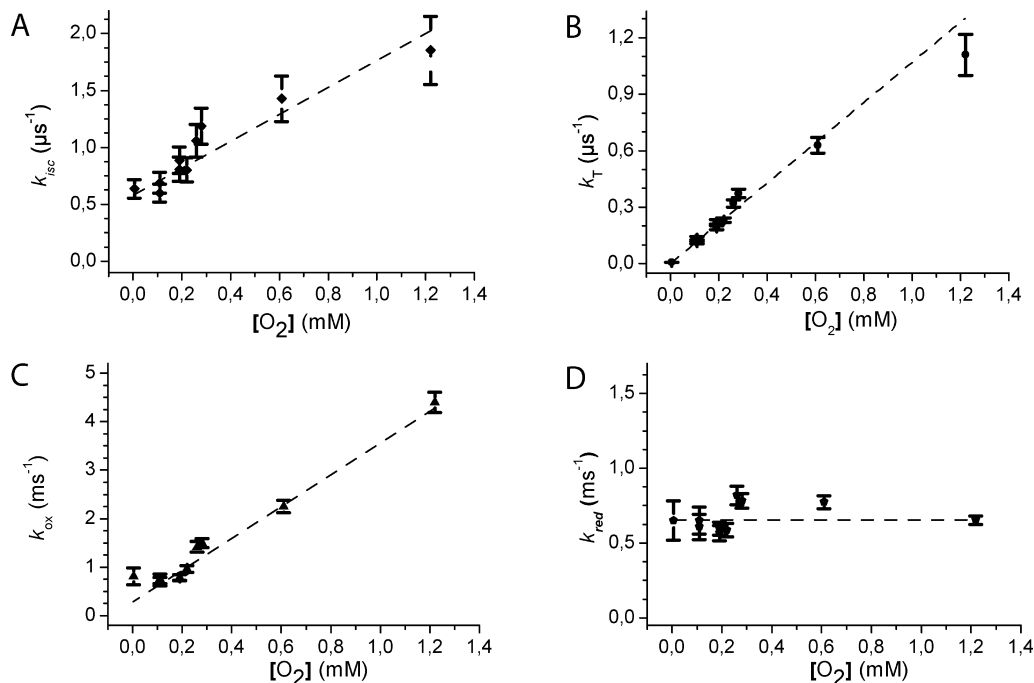


Figure 7. Rates of intersystem crossing k_{isc} , triplet relaxation k_T , oxidation k_{ox} , and reduction k_{red} obtained from $\langle S(w,r) \rangle_w$ measurements and subsequent parameter fitting as a function of the dissolved oxygen concentration in the sample. The reduction rate is constant, whereas the other rates increase linearly. The quenching constants of the other rates are given in Table 1.

When the sample is equilibrated to a pure oxygen atmosphere (Figure 6C–E), the maximum measured triplet amplitude is reduced from about 22% in an air-equilibrated solution to about 12%. This reflects a corresponding difference in the relation between the k_{isc} and k_T rates. The rates extracted by the fit show that upon oxygenation, k_T increased from $k_T = 0.37 \pm 0.02 \mu\text{s}^{-1}$ in air atmosphere to $k_T = 1.1 \pm 0.1 \mu\text{s}^{-1}$, and k_{isc} increased from $k_{\text{isc}} = 1.2 \pm 0.2$ to $1.8 \pm 0.3 \mu\text{s}^{-1}$.

The increase of both of the rates reflects the higher rates of collisional interactions between the dye molecules and dissolved oxygen molecules promoting singlet–triplet transitions in both directions. The oxygen influence was further investigated by systematically varying the oxygen concentration in the samples and repeating the measurements. The resulting extracted parameters are summarized in Figure 7, which shows that both the intersystem crossing and the triplet relaxation rates increase

TABLE 3: Values Obtained for the Quenching Constants of Oxygen for the S_1-T and $T-S_0$ Transitions^a

	k_Q (exp) $\times 10^8$ [1/(s M)]	k_Q (ref) $\times 10^8$ [1/(s M)]	k_0 (exp) $\times 10^5$ [1/s]	k_0 (ref) $\times 10^5$ [1/s]
k_{isc}	11.9 ± 2.1	$(10 \pm 3)^{20}$ 22 ⁴⁸ 9 ¹⁵	5.8 ± 0.5	6.1^{48}
k_T	10.7 ± 0.2	$(18 \pm 2)^{20}$ 22 ⁴⁸	0.11 ± 0.04	0.59^{48}

^a Experimental (exp) values are for Rh110 in PBS under modulated TIR excitation, whereas reference values are for Rh6G in water.

TABLE 4: Values Obtained for the Quenching Constants of Oxygen for the $T-R$ Transitions^a

	k_Q (exp) $\times 10^6$ [1/(s M)]	k_0 (exp) $\times 10^2$ [1/s]
k_{ox}	3.3 ± 0.3	2.7 ± 0.8

^a Experimental (exp) values are for Rh110 in PBS under modulated TIR excitation.

linearly with dissolved oxygen in the solution. Their quenching constants for oxygen ($k_{Q_{\text{isc}}}$ and k_{Q_T}), given by the slopes of Figure 7A and B and according to Stern–Volmer theory,²⁰ are presented in Table 3. Interestingly, also for the oxidation rate, a linear Stern–Volmer behavior could be extracted, as summarized in Table 4.

Influence of Ascorbic Acid as Reducing Agent. To investigate the sensitivity of the presented method to reducing agents, measurements were performed at different ascorbic acid concentrations. In Figure 8A and D, a set of $\langle S(w,r) \rangle_w$ curves is shown for Rh110 in PBS buffer in the presence of 2 and 7 μM ascorbic acid, respectively. From the recorded set of curves and the corresponding T_1 and \dot{R}^+ images (Figure 8B,E and C,F, respectively), the radical state population can be seen to decrease upon addition of ascorbic acid, while the triplet-state population remains essentially unaffected. In the parameter fitting of the $\langle S(w,r) \rangle_w$ curves, the decrease of the radical state decay

amplitude with increasing ascorbic acid concentrations made it difficult to fit both the oxidation and the reduction rates to the measurement data. Assuming the k_{ox} rate to be independent of the ascorbic acid concentration, the k_{ox} rates of the different radial shells were fixed to the values obtained for that shell from a measurement without reducing agent. For the ascorbic acid concentration measurements at 2 and 7 μM , as shown in Figure 8A and 8D, parameter fitting yielded reduction rates of $k_{\text{red}} = 1.2 \pm 0.1 \text{ ms}^{-1}$ and $k_{\text{red}} = 2.2 \pm 0.3 \text{ ms}^{-1}$, respectively. The triplet parameters from the fit were found to be well in agreement with the values obtained previously in an air atmosphere and in the absence of ascorbic acid. Figure 9 summarizes the fitted parameters from measurements at a series of different ascorbic acid concentrations. The fitted parameters confirm that there is no effect of ascorbic acid on the triplet-state parameters (Figure 9A and B). In contrast, the reduction rate was found to display a close to linear increase with increasing ascorbic acid concentrations, with a slope of $(2.6 \pm 0.3) \times 10^8 \text{ M}^{-1} \text{ s}^{-1}$. This is almost an order of magnitude lower than the corresponding value for Rh6G ($1.3 \times 10^9 \text{ M}^{-1} \text{ s}^{-1}$) determined by confocal FCS measurements.²³ Electron-transfer reactions involving aromatic dye molecules typically take place on short molecular scales.^{43,44} The lower rate of Rh110 can thus be a consequence of its lower hydrophobicity compared to that

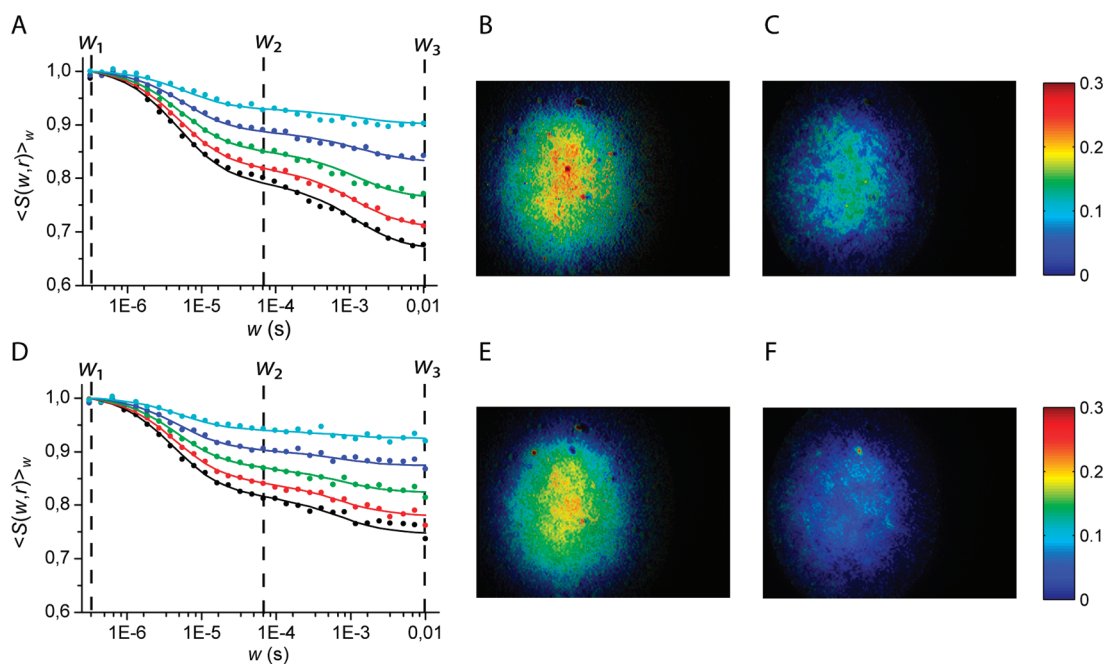


Figure 8. (A) $\langle S(w,r) \rangle_w$ measurements of Rh110 in PBS in the presence of 2 μM ascorbic acid. Points and curves show the response and fit of a few selected regions at different excitation intensities. The fit gives $k_{\text{isc}} = 1.0 \pm 0.1 \text{ } \mu\text{s}^{-1}$, $k_T = 0.26 \pm 0.01 \text{ } \mu\text{s}^{-1}$, $k_{\text{ox}} = 1.1 \text{ ms}^{-1}$ (fixed), and $k_{\text{red}} = 1.2 \pm 0.1 \text{ ms}^{-1}$. (B, C) T_1 and \dot{R}^+ images for a Rh110, 2 μM ascorbic acid solution generated by use of eqs 16 and 17, respectively, and from images recorded at the pulse widths w_1 , w_2 , and w_3 , as indicated in (A). (D) Corresponding measurements and fitting outcome for a solution containing 7 μM ascorbic acid. Fitting parameters: $k_{\text{isc}} = 1.0 \pm 0.1 \text{ } \mu\text{s}^{-1}$, $k_T = 0.3 \pm 0.02 \text{ } \mu\text{s}^{-1}$, $k_{\text{ox}} = 1.1 \text{ ms}^{-1}$ (fixed), and $k_{\text{red}} = 2.2 \pm 0.3 \text{ ms}^{-1}$. (E, F) Corresponding images for the 7 μM ascorbic acid solution T_1 and \dot{R}^+ images. The pulse widths used are indicated in (D). The color scales in (B), (C), (E), and (F) denote average relative populations during active excitation.

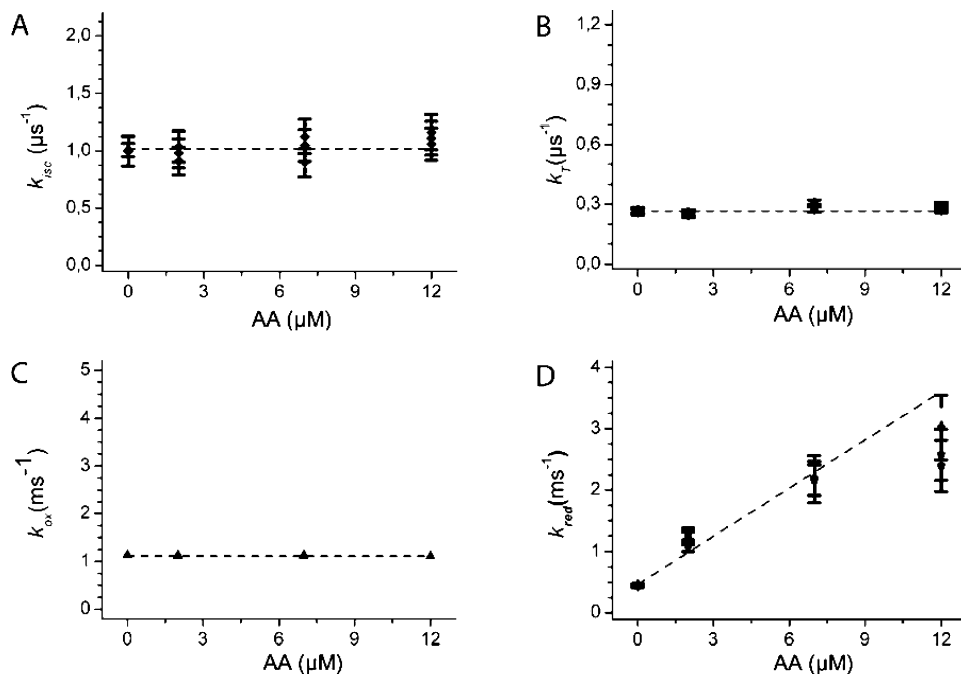


Figure 9. Rates of intersystem crossing k_{isc} , triplet relaxation k_T , oxidation k_{ox} , and reduction k_{red} obtained from $\langle S(w,r) \rangle_w$ measurements and subsequent parameter fitting as a function of the ascorbic acid concentration in the solution. The triplet parameters did not change with ascorbic acid concentration. The oxidation rate, k_{ox} , has been fixed to 1.2 ms^{-1} . The measured reduction rates, k_{red} , increased close to linearly with the ascorbic acid concentration. By linear regression, omitting the value for the highest ascorbic acid concentration yields a slope of $(2.6 \pm 0.3) \times 10^8 \text{ M}^{-1} \text{ s}^{-1}$.

of Rh6G. Rh110 would then less readily form hydrophobic complexes with ascorbic acid, which is likely to be the major rate-limiting step for the electron transfer to take place.²² It should also be noted that the measurements in this study monitor the electron-transfer reactions close to a dielectric surface. The effective concentration of ascorbic acid close to the surface may be lower than that in the bulk, which would also contribute to the lower reduction quenching rate.

Conclusion

In this work, we present a new approach which combines transient state (TRAST) monitoring with total internal reflection (TIR) fluorescence microscopy. By a time-modulated surface-confined TIR excitation field, photoinduced, long-lived, and therefore highly environmentally sensitive states of fluorescent molecules close to the glass surface can be monitored in a parallel manner by a standard CCD camera. At the same time, by this confinement, in combination with the low duty cycles of excitation, the overall photodegradation of the fluorescent molecules of the sample can be kept low.

The approach is based on instrumentation with no or minor requirements on detection sensitivity and time resolution. Unlike fluorescence-based single-molecule or fluctuation approaches like FCS, the presented approach does not rely on the ability to accurately record fluorescence time traces, reflecting the spontaneous blinking behavior of an individual or a very low number of fluorescent molecules to retrieve the transient state information. The approach is therefore not restricted to samples with a high fluorescent brightness and can be applied over a broad range of sample concentrations. Like transient state monitoring by FCS, the presented approach combines the signal strength of fluorescence with the environmental sensitivity of long-lived nonfluorescent states. For both approaches, the transient state information is extracted from the probability of detecting a fluorescent photon from a fluorescent species at a certain time

after the fluorescent molecule was found in its ground state, S_0 . Unlike FCS, however, this probability is reflected by the associated decay of the average fluorescence with increasing excitation pulse widths and not by the correlation in time between spontaneously emitted photons from one and the same fluorophore. The observation time window is therefore not limited by the molecular passage times, as it is in FCS. Thereby, not only triplet states but also photo-oxidized states can be monitored, whose lifetimes typically by far exceed the average dwell times of the fluorophores in the TIR excitation volume.

The validity of the approach was tested both by simulations and experiments. For the dye Rh110 in aqueous solution, two distinct decays could be observed in the fluorescence response curves, which were analyzed upon systematic variation of the concentrations of oxygen and ascorbic acid, known to influence the triplet and photo-oxidized states of this dye. From the analyses, on the basis of a simplified three-state photodynamic model, the triplet-state parameters could be accurately determined. On the other hand, the photo-oxidation rates, k_{ox} , were underestimated by approximately a factor of 2, and the reduction rates, k_{red} , were overestimated by up to a factor of 5. We attribute these deviations to diffusion of the fast, freely diffusing dyes investigated here. For more slowly diffusing species, like large or membrane-bound proteins, computer simulations show that the proposed model provides accurate estimates also of the redox rates. From the simulation, it can also be concluded that although the approach does not provide accurate redox rates for fast diffusing species, relative changes in redox rates are well reflected. It can also be noted that if the redox properties are known, the influence of diffusion on the measured redox rates can allow the mobility of the fluorescent species in the sample to be determined.

The population and kinetics of the triplet and photo-oxidized states monitored by our approach strongly depend on the oxygen content and the redox environment. It is therefore interesting

to consider the use of this approach for monitoring, and imaging these properties in biology. Very recently, TRAST imaging by modulated wide-field excitation was applied to monitor the oxygen consumption upon contraction of individual smooth muscle cells.⁴⁵ On a cellular level, a range of diseases, including inflammatory, metabolic, and malignant diseases, manifest themselves by local changes in the intracellular redox environment. The interior of a living cell obviously presents a more complex measurement medium than a homogeneous solution. In particular, the limited reservoir volumes of the cell or cellular organelles may lead to depletion of fluorescent molecules due to photobleaching.^{46,47} Although TIR-mediated confinement of the excitation volume to the very surface reduces this depletion, absolute measurements of redox environments in living cells require careful control and calibration. Even if absolute determination of redox rates in cells would prove difficult, we believe that our approach can provide a simple and sensitive means to image and analyze relative changes, both for diagnostic purposes as well as for fundamental studies of the underlying complex regulation mechanisms.

Acknowledgment. This study was supported by funds from the European Union 7th Framework Programme (FLUODIAMON 201 837) and by the Knut and Alice Wallenberg Foundation. H.B. acknowledges the financial support of the Swedish Research Council (VR-671-2006-3197). We thank Per Thyberg for fruitful discussions about data analysis.

Supporting Information Available: Additional information as noted in the text. This material is available free of charge via the Internet at <http://pubs.acs.org>.

References and Notes

- (1) Suhling, K.; French, P. M. W.; Phillips, D. *Photochem. Photobiol. Sci.* **2005**, *4*, 13–22.
- (2) Schäferling, M.; Nagl, S. *Anal. Bioanal. Chem.* **2006**, *385*, 500–517.
- (3) Widengren, J.; Kudryavtsev, V.; Antonik, M.; Berger, S.; Gerken, M.; Seidel, C. A. M. *Anal. Chem.* **2006**, *78*, 2039–2050.
- (4) Kudryavtsev, V.; Felekyan, S.; Wozniak, A. K.; Konig, M.; Sandhagen, C.; Kuhnemuth, R.; Seidel, C. A. M.; Oesterhelt, F. *Anal. Bioanal. Chem.* **2007**, *387*, 71–82.
- (5) Donnert, G.; Eggeling, C.; Hell, S. W. *Photochem. Photobiol. Sci.* **2009**, *8*, 481–485.
- (6) Eggeling, C.; Widengren, J.; Rigler, R.; Seidel, C. A. M. *Anal. Chem.* **1998**, *70*, 2651–2659.
- (7) Widengren, J.; Rigler, R. *Bioimaging* **1996**, *4*, 149–157.
- (8) Lippincott-Schwartz, J.; Altan-Bonnet, N.; Patterson, G. H. *Nat. Rev. Mol. Cell Biol.* **2003**, *S7*–S14.
- (9) Hell, S. W. *Science* **2007**, *316*, 1153–1158.
- (10) Hell, S. W.; Kroug, M. *Appl. Phys. B* **1995**, *60*, 495–497.
- (11) Betzig, E.; Patterson, G. H.; Sougrat, R.; Lindwasser, O. W.; Olenych, S.; Bonifacino, J. S.; Davidson, M. W.; Lippincott-Schwartz, J.; Hess, H. F. *Science* **2006**, *313*, 1642–1645.
- (12) Rust, M. J.; Bates, M.; Zhuang, X. W. *Nat. Methods* **2006**, *3*, 793–795.
- (13) van Amerongen, H.; van Grondelle, R. *Methods Enzymol.* **1995**, *246*, 201–226.
- (14) Chen, E.; Chance, M. R. *Methods Enzymol.* **1993**, *226*, 119–147.
- (15) Korobov, V. E.; Chibisov, A. K. *J. Photochem.* **1978**, *9*, 411–424.
- (16) Jovin, T. M.; Vaz, W. L. *Methods Enzymol.* **1989**, *172*, 471–513.
- (17) Cioni, P.; Strambini, G. B. *Biochim. Biophys. Acta* **2002**, *1595*, 116–130.
- (18) Marriott, G.; Clegg, R. M.; Arndtjovin, D. J.; Jovin, T. M. *Biophys. J.* **1991**, *60*, 1374–1387.
- (19) Widengren, J.; Rigler, R.; Mets, Ü. *J. Fluoresc.* **1994**, *4*, 255–258.
- (20) Widengren, J.; Mets, Ü.; Rigler, R. *J. Phys. Chem.* **1995**, *99*, 13368–13379.
- (21) Widengren, J.; Schwille, P. *J. Phys. Chem. A* **2000**, *104*, 6416–6428.
- (22) Widengren, J.; Dapprich, J.; Rigler, R. *Chem. Phys.* **1997**, *216*, 417–426.
- (23) Widengren, J.; Chmyrov, A.; Eggeling, C.; Löfdahl, P. A.; Seidel, C. A. M. *J. Phys. Chem. A* **2007**, *111*, 429–440.
- (24) Widengren, J.; Schweinberger, E.; Berger, S.; Seidel, C. A. M. *J. Phys. Chem. A* **2001**, *105*, 6851–6866.
- (25) Hassler, K.; Leutenegger, M.; Rigler, P.; Rao, R.; Rigler, R.; Gösch, M.; Lasser, T. *Opt. Express* **2005**, *13*, 7415–7423.
- (26) Hassler, K.; Rigler, P.; Blom, H.; Rigler, R.; Widengren, J.; Lasser, T. *Opt. Express* **2007**, *15*, 5366–5375.
- (27) Blom, H.; Chmyrov, A.; Hassler, K.; Davis, L. M.; Widengren, J. *J. Phys. Chem. A* **2009**, *113*, 5554–5566.
- (28) Koppel, D. E. *Phys. Rev. A* **1974**, *10*, 1938–1945.
- (29) Kannan, B.; Guo, L.; Sudhaharan, T.; Ahmed, S.; Maruyama, I.; Wohland, T. *Anal. Chem.* **2007**, *79*, 4463–4470.
- (30) Kolin, D. L.; Ronis, D.; Wiseman, P. W. *Biophys. J.* **2006**, *91*, 3061–3075.
- (31) Sankaran, J.; Manna, M.; Guo, L.; Kraut, R.; Wohland, T. *Biophys. J.* **2009**, *97*, 2630–2639.
- (32) Blom, H.; Gösch, M. *Curr. Pharm. Biotechnol.* **2004**, *5*, 231–241.
- (33) Sanden, T.; Persson, G.; Thyberg, P.; Blom, H.; Widengren, J. *Anal. Chem.* **2007**, *79*, 3330–3341.
- (34) Sanden, T.; Persson, G.; Widengren, J. *Anal. Chem.* **2008**, *80*, 9589–9596.
- (35) Penzkofer, A.; Beidoun, A. *Chem. Phys.* **1993**, *177*, 203–216.
- (36) Ermolaev, V. L.; Lyubimtsev, V. A. *Opt. Spektrosk.* **1984**, *56*, 1026–1032.
- (37) Mertz, J. *J. Opt. Soc. Am. B* **2000**, *17*, 1906–1913.
- (38) Sonesson, A. W.; Blom, H.; Hassler, K.; Elofsson, U. M.; Callisen, T. H.; Widengren, J.; Brismar, H. *J. Colloid Interface Sci.* **2008**, *317*, 449–457.
- (39) Plaetzer, K.; Krammer, B.; Berlanda, J.; Berr, F.; Kiesslich, T. *Lasers Med. Sci.* **2009**, *24*, 259–268.
- (40) Müller, C. B.; Loman, A.; Pacheco, V.; Koberling, F.; Willbold, D.; Richtering, W.; Enderlein, J. *Europhys. Lett.* **2008**, *83*, 46001.
- (41) Leutenegger, M.; Blom, H.; Widengren, J.; Eggeling, C.; Gösch, M.; Leitgeb, R. A.; Lasser, T. *J. Biomed. Opt.* **2006**, *11*, 040502.
- (42) Hübner, C. G.; Renn, A.; Renge, I.; Wild, U. P. *J. Chem. Phys.* **2001**, *115*, 9619–9622.
- (43) Sauer, M.; Han, K.-T.; Müller, R.; Nord, S.; Schulz, A.; Seeger, S.; Wolfrum, J.; Arden-Jacob, J.; Deltau, G.; Marx, N. J.; Zander, C.; Drexhage, K. H. *J. Fluoresc.* **1995**, *5*, 247–261.
- (44) Rehm, D.; Weller, A. *Isr. J. Chem.* **1970**, *259*–271.
- (45) Geissbuehler, M.; Spielmann, T.; Formey, A.; Märki, I.; Leutenegger, M.; Hinz, B.; Johnsson, K.; Van De Ville, D.; Lasser, T. *Biophys. J.* **2010**, *98*, 339–349.
- (46) Delon, A.; Usson, Y.; Derouard, J.; Biben, T.; Souchier, C. *J. Fluoresc.* **2004**, *14*, 255–267.
- (47) Widengren, J.; Thyberg, P. *Cytometry, Part A* **2005**, *68A*, 101–112.
- (48) Gregor, I.; Heupel, M.; Thiel, E. *Chem. Phys.* **2001**, *272*, 185–197.